

Numerical study of the topological Anderson insulator in HgTe/CdTe quantum wells

Hua Jiang¹, Lei Wang¹, Qing-feng Sun¹, and X. C. Xie^{2,1}

¹*Beijing National Lab for Condensed Matter Physics and Institute of Physics,
Chinese Academy of Sciences, Beijing 100190, China;*

²*Department of Physics, Oklahoma State University, Stillwater, Oklahoma 74078*

(Dated: May 28, 2009)

We study the disorder effect on the transport properties in the HgTe/CdTe semiconductor quantum wells. We confirm that at a moderate disorder strength, the initially un-quantized two terminal conductance becomes quantized, and the system makes a transition to the novel topological Anderson insulator (TAI). Conductances calculated for the stripe and cylinder samples reveal the topological feature of TAI and supports the idea that the helical edge states may cause the anomalous quantized plateaus. The influence of disorder is studied by calculating the distributions of local currents. Base on the above-mentioned picture, the phenomena induced by disorder in the quantum spin Hall region and TAI region are directly explained. Our study of the local current configurations shed further light on the mechanism of the anomalous plateau.

PACS numbers: 73.43.Nq, 72.15.Rn, 72.25.-b, 85.75.-d

I. INTRODUCTION

Quantum spin Hall effect (QSHE), which is proposed as a new class of topological state of matter in two dimensions, has generated a great deal of interest¹. Contrary to the integer or the fractional quantum Hall state, which is induced by a magnetic field that breaks the time reversal symmetry, QSHE is caused by a strong spin-orbit interaction that maintains the time reversal symmetry. Kane and Mele proposed a Z_2 classification for this kind of the new topological state². For materials with spatial inversion symmetry, the index could be easily computed as the product of parities of the wave function at several high symmetry points in the Brillouin zone. The Z_2 classification can be generalized to three-dimensional systems as well³. Recently, topological insulators suitable for room temperature applications are also predicted⁴. The QSH state has the helical edge states, namely, having two counter-propagating edge states for the two opposite spin polarizations. The helical edge states are stable against time-reversal conserving perturbations, since backscattering processes need to connect the upper and lower edges of the sample. The probability of backscattering is exponentially suppressed as the sample width is increased. Recent experiment⁵ provides evidences of the QSHE in HgTe/CdTe quantum well (QW) structures, as predicted theoretically⁶. The de-coherence effect in QSH samples is also investigated.⁷ Some interesting questions emerge such as the response of a QSH state to the disorder, and the interplay of the helical edge states and the bulk states.

According to the celebrated scaling argument, in two dimensions the bulk electron wave functions are localized in the presence of any weak disorder⁸. But there are two known exceptions, one is the two dimensional systems with a strong spin-orbital coupling, and the other is the quantum Hall transition between different plateaus⁹. With the discover of QSHE state in two dimensions, study of the localization is in demand. Sheng

et al investigated the disorder effect in honeycomb lattice QSHE sample, they found the QSHE phase is robust against weak disorder¹⁰. Ono and Obuse *et al* studied the critical properties of the transition from a metal to a QSH state, and they found the results to be somewhat controversial^{11,12}.

Recently, Li¹³ *et al* studied the transport properties of the HgTe/CdTe QWs in the presence of disorder, they found as the increasing of the disorder strength, the initially un-quantized conductance became quantized, *i.e.* the sample enters into the QSH state because of the disorder, so they named the state as "topological Anderson insulator"(TAI). The newly anomalous quantized conductance plateau is caused by the edge transport, which is indirectly revealed by the unchanged plateau value along with width variation for two-terminal calculation and quantized transmission coefficient for four-terminal calculation. However, the detailed mechanics of the edge transport is less clear.

In the present paper, we study the effect of disorder on the electronic state of HgTe/CdTe QWs. We carry out Keldysh's nonequilibrium-Green-function (NEGF) calculations based on a four-band tight binding model. First, we perform the conductance calculations for two different geometries. In the case of a stripe geometry(see fig. 1(a)), the presence of the helical edge states are evident from the band spectrum, the TAI phase described in reference 12 appears. While for the cylindrical geometry, *i.e.* periodical boundary condition along y direction(see fig. 1(b)), there is no edge state, the bulk state is localized by disorder and there is no quantized conductance. These results strongly support the thesis that anomalous conductance plateau is due to the edge transport and give a better understanding of the topological feature of the TAI phase. Second, we obtain the distributions of the local currents for the two-terminal strip samples with different chemical potentials and disorder strengths. The evolvement of the local current vector configurations gives rise to a direct demonstration of the impurity influ-

ence in the HgTe/CdTe QWs. By analyzing these local current configurations, the transport phenomena in both normal QSH region and TAI region are clearly explained. Moreover, the detailed results, such as the coexistence of the bulk and edge states at the dip point (see Fig.6) and the bulk states assisted backscattering obtained from the local current vector configurations shed further light on the mechanism of the disorder induced edge states for the TAI.

The rest of this paper is organized as follows. In Section II, we introduce the effective tight-binding model. The formulas and calculation method are also described. In Section III, the numerical results and their discussions are presented. Finally, a conclusion is given in Section IV.

II. THE MODEL AND METHOD

As a starting point, we introduce the effective Hamiltonian for the HgTe/CdTe QWs with Anderson impurity in the tight-binding representation. We consider a square lattice with four special orbit states $|s, \uparrow\rangle, |p_x + ip_y, \uparrow\rangle, |s, \downarrow\rangle, |-(p_x - ip_y), \downarrow\rangle$ on each site. Here \uparrow, \downarrow denotes the electron spin. Through symmetry consideration, the effective Hamiltonian can be written as^{5,6,13,14}

$$\begin{aligned}
 H = & \sum_{\mathbf{i}} \varphi_{\mathbf{i}}^{\dagger} \begin{pmatrix} E_{isa} & 0 & 0 & 0 \\ 0 & E_{ipc} & 0 & 0 \\ 0 & 0 & E_{isb} & 0 \\ 0 & 0 & 0 & E_{ipd} \end{pmatrix} \varphi_{\mathbf{i}} \\
 & + \sum_{\mathbf{i}} \varphi_{\mathbf{i}}^{\dagger} \begin{pmatrix} V_{ss} & V_{sp} & 0 & 0 \\ -V_{sp}^* & V_{pp} & 0 & 0 \\ 0 & 0 & V_{ss} & V_{sp}^* \\ 0 & 0 & -V_{sp} & V_{pp} \end{pmatrix} \varphi_{\mathbf{i}+\delta x} + h.c. \\
 & + \sum_{\mathbf{i}} \varphi_{\mathbf{i}}^{\dagger} \begin{pmatrix} V_{ss} & iV_{sp} & 0 & 0 \\ iV_{sp}^* & V_{pp} & 0 & 0 \\ 0 & 0 & V_{ss} & -iV_{sp}^* \\ 0 & 0 & -iV_{sp} & V_{pp} \end{pmatrix} \varphi_{\mathbf{i}+\delta y} + h.c.
 \end{aligned} \quad (1)$$

Here $\mathbf{i} = (ix, iy)$ is the site index, and δx and δy are unit vectors along the x and y directions. $\varphi_{\mathbf{i}} = (a_i, c_i, b_i, d_i)^T$ represents the four annihilation operators of electron on the site \mathbf{i} with the state indexes $|s, \uparrow\rangle, |p_x + ip_y, \uparrow\rangle, |s, \downarrow\rangle, |-(p_x - ip_y), \downarrow\rangle$, respectively. The on-site matrix elements satisfy $E_{isa} = E_s + W_{isa}, E_{ipc} = E_p + W_{ipc}, E_{isb} = E_s + W_{isb}, E_{ipd} = E_p + W_{ipd}$. $W_{isa}, W_{ipb}, W_{isc}$, and W_{ipd} are on-site disorder energies uniformly distributed in the range $[-\frac{W}{2}, \frac{W}{2}]$ with the disorder strength W . E_s, E_p, V_{ss}, V_{pp} , and V_{sp} are the five independent parameters that characterize the clean HgTe/CdTe samples. It is clear that near the Γ point the lattice Hamiltonian (Eq. (1)) in k -representation can be reduced to the continuous Hamiltonian in Ref.6 when we take $V_{sp} = -iA/2a$, $V_{ss} = (B + D)/a^2$, $V_{pp} = (D - B)/a^2$, $E_s = C + M -$

$4(B + D)/a^2$, and $E_p = C - M - 4(D - B)/a^2$. Here a is the lattice constant and all the parameters A, B, C, D, M can be controlled experimentally⁵. Moreover, the Eq.(1) can be directly obtained by discretizing spatial coordinates of the continuous Hamiltonian using the substitution $k_x \rightarrow -i\frac{\partial}{\partial x}, k_y \rightarrow -i\frac{\partial}{\partial y}$.¹⁵

In this paper, we apply the model to two geometric devices. The device a (see fig. 1(a)) is of stripe geometry, while the device b (see fig. 1(b)) is of cylindrical geometry which can be obtained by rolling the device a into a tube. Without disorder ($W=0$), the energy spectrum of such two geometric devices can be calculated by diagonalizing Eq.(1) using the periodic boundary condition in x direction^{16,17}. Next we investigate how the disorder affects the transport properties of such systems. For both devices a and b, the size of the central region is $L \times W$. For convenience, we assume that the Anderson impurities only exist in the (red) filled region and the temperature is zero.

In our simulations, a small external bias $V = V_L - V_R$ is applied between the two terminals. With the help of the NEGF method, the local current between neighboring sites \mathbf{i} and \mathbf{j} is calculated from the formula^{18,19}

$$J_{\mathbf{i} \rightarrow \mathbf{j}} = \frac{2e^2}{h} \text{Im} \left[\sum_{\alpha, \beta} H_{i\alpha, j\beta} G_{j\beta, i\alpha}^n(E_F) \right] (V_L - V_R) \quad (2)$$

where V_L, V_R are the voltages at the *Lead-L, R*. α, β denote the state indices. $G^n(E_F) = G^r \Gamma_L G^a$ is electron correlation function with line width function $\Gamma_{\alpha}(E_F) = i[\Sigma_{\alpha}^r(E_F) - (\Sigma_{\alpha}^r(E_F))^{\dagger}]$, the Green function $G^r(E_F) = [E_F - H_{cen} - \Sigma_L^r(E_F) - \Sigma_R^r(E_F)]^{-1}$ and the Hamiltonian in the central region denoted as H_{cen} . The retarded self-energy Σ_L^r, Σ_R^r due to the coupling to the lead-*L, R* can be calculated numerically²⁰. Note that for Eq. (1), the spin up (a_i, c_i) subsystem and spin down (b_i, d_i) subsystem are decoupled. The local current between neighboring sites \mathbf{i} and \mathbf{j} with spin index σ $J_{\mathbf{i} \rightarrow \mathbf{j}}^{\sigma}$ can also be calculated from Eq.(2) by summing over only the state index with the corresponding unitary subsystem. The current J_L flowing through the device is calculated by summing all the local current $J_{\mathbf{i} \rightarrow \mathbf{i}+\delta x}$ for an arbitrary column. After obtaining the current J_L , the linear conductance G_{LR} is given by $G_{LR} = J_L / (V_L - V_R)$. In addition, the linear conductance can be directly obtained by $G_{LR} = \text{Tr}[\Gamma_L G^r \Gamma_R G^a]$. The agreement between the two methods gives strong confirmation of our analytical derivations and numerical calculations.

In the following numerical calculations, we choose the realistic material parameters A, B, C, D, M that arrived from the HgTe/CdTe QWs.⁵ The sample width (or circumference) is fixed to $L_y = 80a$ with the lattice constant $a = 5nm$. Since the model is only valid in small k , we confine the Fermi energy within a small region near the Γ point. In the presence of disorder, the conductance G , conductance fluctuation δG , the local current $J_{\mathbf{i} \rightarrow \mathbf{j}}^{\sigma}$ etc., are all averaged over up to 500 random configurations.

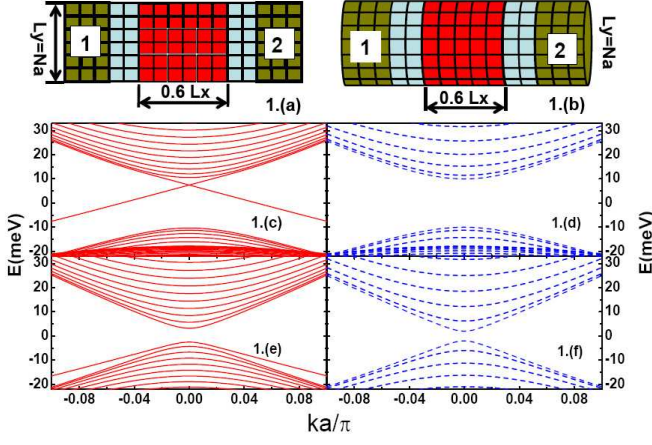


FIG. 1: (color online) (a) and (b) are the schematic diagrams for two devices. The Anderson impurities only exist in the (red) filled regions. (c) and (e) show the one-dimensional energy bands for device a. The parameters are $A = 3.645\text{eV} \cdot \text{\AA}$, $B = -68.6\text{eV} \cdot \text{\AA}^2$, $C = 0.0\text{meV}$, $D = -51.2\text{eV} \cdot \text{\AA}^2$, and gap parameter $M = -10\text{meV}$ (c), $M = 2\text{meV}$ (e). (d) and (f) demonstrate the one-dimensional energy bands for device b with the same parameters as (c) and (e), respectively.

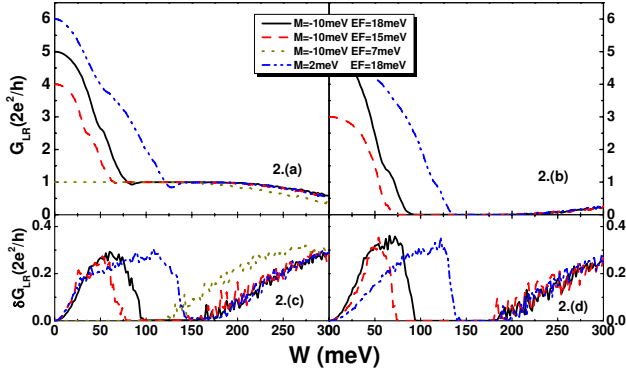


FIG. 2: (color online) The conductance G (a)(b) and conductance fluctuation δG (c)(d) vs disorder strength W for different Fermi energy E_F and gap parameter M . (a)(c) for device a and (b)(d) for device b. The central region length $L_x = 200a$. Other parameters (A , B , C , and D) are the same as fig. 1(c)-1(f).

III. NUMERICAL RESULTS

Let us first compare the two devices in geometry and topology. In device *a* with open boundary (fig.1(a)), there are two edges in the y direction. Thus, the edge states can exist in such device. Since the fig. 1(b) is a cylinder without edge, the edge states are prohibited in the device b. In figures 1(c) and 1(e), the band structures of clean HgTe/CdTe QWs are plotted. There exist a bulk energy gap approximately of $2|M|$ in both figures. Moreover, there are two degenerate bands (edge states) cross inside the gap for gap parameter $M < 0$ (fig. 1(c)). In contrast, the crossing bands vanished when M

was tuned up to above zero (fig. 1(d)). These results are in agreement with those of previous studies^{6,16}. In figures 1(d) and 1(f), we plot the corresponding band structures in the cylindrical geometry. For both gap parameter $|M| > 0$ and $|M| < 0$, though the degeneracy is higher due to the enhanced symmetry, the bulk energy gap is nearly unchanged and there is only tiny shift in the energy bands. However, there is a big difference between the two samples, the edge states which cross inside the gap vanish in the later one. The phenomenon originates from the topology of the device, when the sample is sufficient large, the bulk states are hardly affected by the topology change at the edge while the edge states are totally destroyed. In conclusion, rolling the sample from a strip to a cylinder destroys the edge channels but maintain the bulk state properties.

Next, we investigate how the transport properties are affected by disorder. Fig. 2(a) and 2(c) plot the conductance G and δG versus disorder strength for device a. When the system is in the inverted regime ($M < 0$) with the Fermi energy inside the bulk gap ($E_F = 7\text{meV}$), for a range of disorder strength W , the two terminal conductance is quantized without much fluctuations. Such observation agrees with the previous result that the QSHE is robust against weak disorder^{2,10}. However, when the chemical potential is tuned up into the bulk band region near the Γ point, no matter $M > 0$ or $M < 0$, the new intriguing phenomena emerge. The conductance G decreases while the fluctuation δG increases when the disorder is first applied. When the disorder strength continues to increase, instead of localization, the conductance begins to increase to a quantized value ($2e^2/h$) and maintains at this value for a certain range before eventually decreases. Meanwhile, the conductance fluctuation δG decreases to zero and vanishes for the corresponding W . The anomalous conductance plateau indicates that the sample becomes a topological insulator. More importantly, different from the traditional topological insulator (QHE etc), the quantized value is induced by the impurities. This disorder induced anomalous conductance plateau was discovered in a very recent work.¹³ Naturally, there exists a question: what is the mechanism that causes such an anomalous plateau?

To answer this question, we first examine G and δG as a function of disorder strength for device b using the same parameters as device a [see Figs. 2(b) and 2(d)]. Unlike the device a, the transport properties follow the traditional Anderson metal-insulator transition feature,⁹ and the anomalous conductance plateau is absent. For instance, the conductance monotonously decreases to zero with increase of the disorder strength and the critic disorder strength W_c increases with raising of the Fermi energy. Significantly, the metal-insulator transition point for device b is roughly at the starting point of the anomalous plateau for device a. Take $M = -10\text{meV}$, $E_F = 18\text{meV}$ for example [see black solid line in fig. 2(a) and 2(b)], the anomalous plateau sets up at the disorder strength $W_c \simeq 93\text{meV}$ for device a

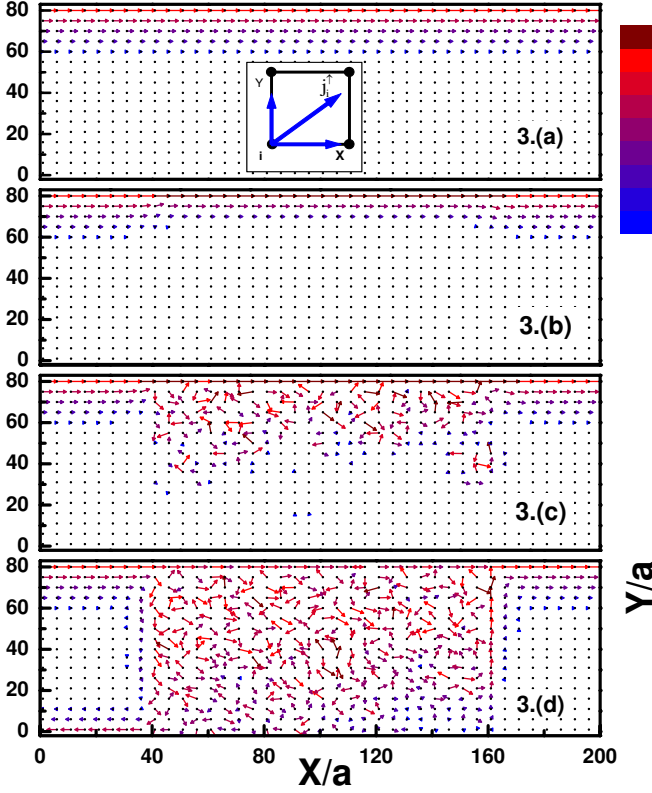


FIG. 3: (color online) Configurations of the local current flow vector for device a with Fermi energy $E_F = 7\text{meV}$, $M = -10\text{meV}$, central region size $L_x = 200a$, $L_y = 80a$ under disorder strength $W=0$ (a) $W=50\text{meV}$ (b) $W=110\text{meV}$ (c) $W=220\text{meV}$ (d). The inset in fig. 3(a) is the schematic of local current flow vector. The vector direction represent the local current flow direction and the vector length is proportional to the logarithm of local current value.

and for that threshold value the device b becomes an insulator ($G \simeq 0$, $\delta G \simeq 0$). As shown in fig. 1, the bulk states in the device a and the device b are the same. Only the edge states are completely destroyed by rolling the device a into the device b. This gives a direct evidence that the anomalous conductance plateau originates from the edge states.

To get a better insight into the microscopic origin of the conductance variations, we examine the disorder effect through the local-current-vector-flow configurations. Due to the time reversal symmetry, we only consider the spin up subsystem, the influence of spin down subsystem can be directly obtained by time reversal symmetry. Here, the local current flow vector on site \mathbf{i} is defined as $J_{\mathbf{i}}^{\uparrow} = J_{\mathbf{i} \rightarrow \mathbf{i} + \delta \mathbf{x}} + J_{\mathbf{i} \rightarrow \mathbf{i} + \delta \mathbf{y}}$.

In fig. 3, the typical distributions of local currents for device a in traditional QSHE region are plotted. For a clean sample (see fig. 3(a)), the local currents locate mainly on the upper edge and their values decay exponentially towards the bulk. Surprisingly, the small disorder initially makes the edge channel narrower (see fig.

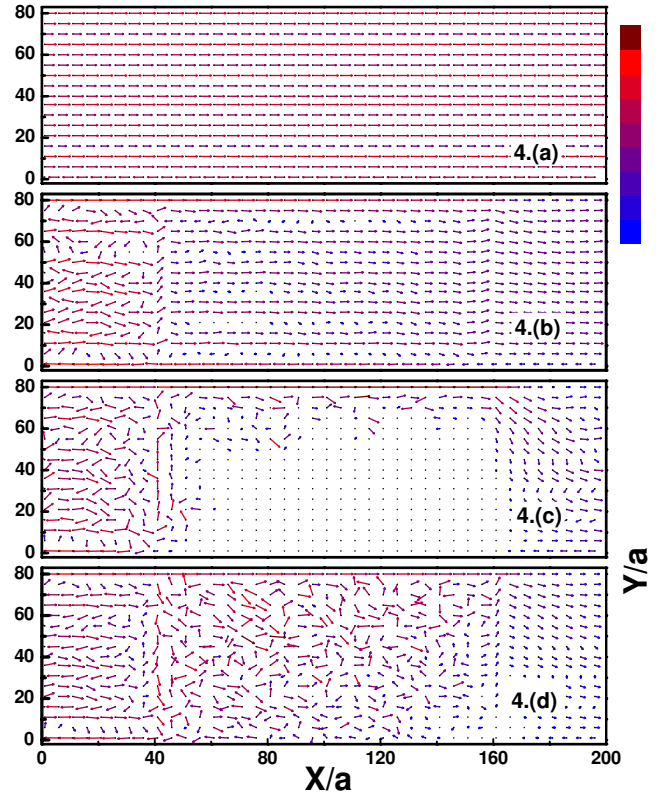


FIG. 4: (color online) Configurations of the local current flow vector for device a with the same sample sizes as for fig. 3, positive gap parameter $M = 2\text{meV}$, Fermi energy $E_F = 18\text{meV}$, and disorder strength $W=0$ (a) $W=100\text{meV}$ (b) $W=150\text{meV}$ (c) $W=250\text{meV}$ (d).

3(b)). Though the mechanism is unclear, we note such phenomenon was also observed recently by Chu *et al.*²¹ In their paper, this narrowing effect was indirectly observed by the decreasing of the oscillation period of the A-B ring, while in this paper such effect is directly shown by the spatial distributions of the local currents. When the Anderson disorder strength is getting larger, the local currents spread to the bulk and broaden the edge channels again (see as fig. 3(c)). However, only when the disorder strength exceeds the critical value W_c , the spread local-current flow can reach the lower edge channels with different chirality, the effective backscattering (as shown in the local current flow vector located near the lower edge in the region $0 < X < 40a$ in fig. 3(d)) can take place, leading to the reduction of the conductance between the two terminals. These pictures explain why the traditional quantized plateau is robust under weak disorder and how it is destroyed in the strong disorder limit.

Next, the Fermi energy is tuned to $E_F = 18\text{meV}$, sitting slightly above the bulk gap. A positive gap parameter $M = 2\text{meV}$, for which there is no helical edge states inside the bulk gap for the clean sample, is chosen in the following simulations. The conductance G vs. disorder strength W shown in fig. 2(a) can be classified to

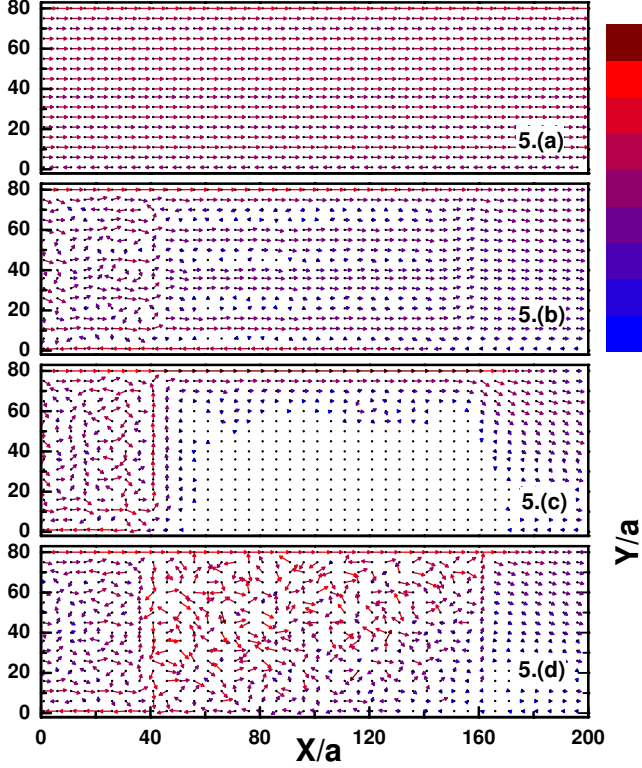


FIG. 5: (color online) Configurations of the local current flow vector for device a with the same sample sizes as for fig. 3, negative gap parameter $M = -10\text{meV}$, Fermi energy $E_F = 18\text{meV}$, and disorder strength $W=0$ (a) $W=65\text{meV}$ (b) $W=100\text{meV}$ (c) $W=250\text{meV}$ (d).

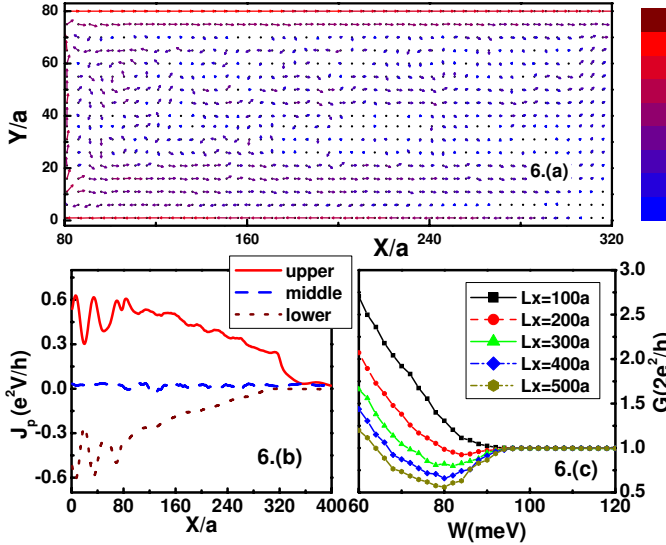


FIG. 6: (color online) (a) Distribution of local currents in the disorder region for device a with length $L_x = 400a$ and $L_y = 80a$ at the dip point. (b) The position-related current J_p vs longitude axis x . J_p is defined as the summation of $j_{i \rightarrow i+\delta x}^\uparrow$ for four layers in the corresponding region. The other parameters are the same as (a). (c) The two-terminal conductance G vs. disorder strength W with different sample lengths L_x .

four regions (i) without disorder, (ii) before the anomalous plateau, (iii) on the anomalous plateau, and (iv) after the anomalous plateau. The typical configurations of local-current-flow vector in such four regions are plotted in fig. 4. For the clean sample (see fig. 4(a)), the local current not only flow forward along the upper edge, but also uniformly flow forward in the bulk. While W is increased from zero into the region (ii), the local currents in the bulk of the disorder region become smaller and more irregular in directions (see fig. 4(b)), which directly shows the decline of the bulk transport and the localization of the bulk states. Fig. 4(c) demonstrates the distribution of the local currents when the device is in the region (iii). The most interesting phenomena exist in the disorder region $X \in [40a, 160a]$. The local currents in the bulk decline to zero while the residual currents flow in the upper edge and flow without much scattering. In addition, throughout the region (iii), the bulk transport vanishes due to the localization of all the bulk states. In contrast, the edge transport shows the same behavior as in the traditional QSHE region: the local currents deeply spread into the bulk without any effective backscattering with W increasing until it connected the opposite edge channels (see as fig. 4(d)). Obviously, such edge transport will lead to the quantized plateau. In the negative gap parameter situation, for example $M = -10\text{meV}$, $E_F = 18\text{meV}$, (see fig. 5) the evolvement of local current configurations resembles that of $M > 0$ situation. So far, the fig. 4(c) and fig. 5(c) are the most strong evidence directly showing that the TAI is caused by the edge transport. In addition, these plots provide a vivid microscopic picture demonstrating the influence of disorder on TAI.

Up to now, we have explained the majority phenomena emerged in the TAI. Nevertheless, the transport properties in the region (ii) of $G - W$ figure demands a detailed study for the following two reasons. (i) The conductance is not monotonously decreasing with increasing disorder strength but shows a dip feature prior to the anomalous plateau. Obviously, at the dip point, the system is neither in TAI phase nor in normal Anderson insulator phase due to its nonzero and non-quantized conductance value. (ii) For both types of gap parameter $M > 0$ and $M < 0$, the dip does exist prior to the anomalous plateau and the conductance G behaves similarly after the dip. Thus, revealing the cause for the dip feature may help us to understand the mechanism of the formation of the edge states.

In fig. 6(a), the distribution of the local currents with the disorder strength W being fixed at the dip is plotted. The local currents flow are larger close to the edges than in the bulk. The predominant edge transport is clearly seen. In fig. 6(b) we plot the position-related current J_p versus longitude axis x . Where J_p is defined as the summation of $j_{i \rightarrow i+\delta x}^\uparrow$ for four layers in the corresponding region. For example, given sample width $L_y = 80a$, J_p for the upper edge is defined as $\sum_{iy=77}^{iy=80} j_{i \rightarrow i+\delta x}^\uparrow$. With the help of J_p , one can quantitatively analyze the local

currents. On the whole, the behavior of the position-related current J_p is similar to the local current configurations, but it is smoother with the position x . More significantly, one can observe from fig. 6(b), the local currents flow from left to right with rapidly decreasing magnitude for upper edge, vice versa for the lower edge. This phenomenon can be attributed to the bulk state assisted backscattering between two edges. The fact that the position-related current J_p in the bulk is small but nonzero indicates that the bulk states are not fully localized at the dip. The scattered carriers in the upper edge can hop through such delocalized bulk states to the lower edge which leads to the backscattering processes. In other words, disorder not only destroys the bulk transport but also quickly destroys the edge transport. Because of this, the conductance G is lower than plateau value at the dip point. For the region after dip (see fig. 2(a)), increasing of W slowly destroys the bulk transport, but it also suppresses the bulk-assisted backscattering mechanism at the same time. It leads to an overall increase of the conductance G . When the bulk states become fully localized, the anomalous plateau shows up. In fig.6(c), the conductance G versus W with different sample lengths L_x are plotted. The dip feature is clearer for a large L_x because of the increasing probability of the backscattering between the two edges. However, for all L_x , the anomalous plateaus appear with the same disorder strength due to the fully localized bulk states.

IV. CONCLUSIONS

In summary, the disorder effect in HgTe/CdTe quantum wells is studied. We confirm the existence of the

topological Anderson insulator(TAI) phase. Conductances calculated for the stripe and cylinder samples reveal the topological feature of TAI and support the idea that helical edge states cause the anomalous quantized plateau. With the help of local-current-vector configurations for different chemical potentials and disorder strengths, the basic physical phenomena emerged in the normal QSHE region and in the TAI region are clearly understood. In particular, the analysis of the local current configurations provides us with the importance of the bulk-states-assisted backscattering in TAI that in turn help us to understand the mechanism of the formation of the disorder induced edge states.

V. ACKNOWLEDGEMENT

The work is supported by NSFC under Grant Nos. 10525418, 10734110, and 10821403, and by 973 Program Project No. 2009CB929101. XCX is supported by US-DOE and Oklahoma C-Spin Center. We thank J. K. Jain, S.Q. Shen, Xuele Liu and Waigen Zhang for helpful discussions. Part of the calculations was performed on the HPCC clusters at OSU.

-
- ¹ For a brief review, see C. Day, *Physics Today* **61** 19 (2008); N. Nagaosa, *Science* **318**, 758 (2007).
 - ² C. L. Kane and E. J. Mele, *Phys. Rev. Lett.* **95** 226801 (2005); C. L. Kane and E. J. Mele, *ibid* **95** 146802 (2005).
 - ³ D. Hsieh, D. Qian, L. Wray, Y. Xia, Y. S. Hor, R. J. Cava and M. Z. Hasan, *Nature(London)* **452**, 970 (2008); Liang Fu, C. L. Kane and E. J. Mele, *Phys. Rev. Lett.* **98**, 106803 (2007).
 - ⁴ Haijun Zhang, Chao-Xing Liu, Xiao-Liang Qi, Xi Dai, Zhong Fang, S. C. Zhang, arxiv: 0812.1622v1; accept by *Nature Physics*; Y. Xia, L. Wray, D. Qian, D. Hsieh, A. Pal, H Lin, A. Bansil, D. Grauer, Y. S. Hor, R. J. Cave, and M. Z. Hasan, arXiv:0812.2078v1.
 - ⁵ M. König, Steffen Wiedmann, Christoph Bruene, Andreas Roth, Hartmut Buhmann, Laurens W. Molenkamp, Xiao-Liang Qi and S. C. Zhang *Science* **318**, 766 (2007); M. König, Hartmut Buhmann, Laurens W. Molenkamp, T. L. Hughes, Chao-Xing Liu, Xiao-Liang Qi and S. C. Zhang *J. Phys. Soc. Jpn.* **77**, 031007 (2008).
 - ⁶ B. A. Bernevig, T. L. Hughes, and S. C. Zhang, *Science* **314**, 1757 (2006).
 - ⁷ Hua Jiang, Shuguang Cheng, Qing-feng Sun and X.C Xie, arxiv0811.1610v1.
 - ⁸ E. Abrahams, P. W. Anderson, D. C. Licciardello and T. V. Ramakrishnan, *Phys. Rev. Lett.* **42**, 673 (1979).
 - ⁹ For a brief review, see F. Evers, A. D. Mirlin, *Rev. Mod. Phys.* **80**, 1355 (2008) and its reference.
 - ¹⁰ L. Sheng, D. N. Sheng, C. S. Ting, and F. D. M. Haldane, *Phys. Rev. Lett.* **95**, 136602 (2005).
 - ¹¹ M. Onoda, Y. Avishai and N. Nagaosa, *Phys. Rev. Lett.* **98**, 076802 (2008).
 - ¹² H. Obuse, Akira Furusaki, Shinsei Ryu, and Christopher Mudry, *Phys. Rev. B* **78**, 115301 (2008); H. Obuse, Akira Furusaki, Shinsei Ryu, and Christopher Mudry, *ibid.* **78**, 115301 (2008).
 - ¹³ Jian Li, Rui-Lin Chu, J. K. Jain, and Shun-Qing Shen, *Phys. Rev. Lett.* **102**, 136806 (2009).
 - ¹⁴ Chao-Xing Liu, Xiao-Liang Qi, Xi Dai, Zhong Fang, and Shou-Cheng Zhang, *Phys. Rev. Lett.* **101**, 146802(2008).
 - ¹⁵ *Electronic Transport in Mesoscopic Systems*, edited by S. Datta (Cambridge University Press 1995).
 - ¹⁶ Xiao-liang Qi, T. L. Hughes and S. C. Zhang *Phys. Rev. B* **78**, 195424 (2008).
 - ¹⁷ Y. Hatsugai, *Phys. Rev. B* **48**, 11851 (1993).

- ¹⁸ A.-P. Jauho, N.S. Wingreen, and Y. Meir, Phys. Rev. B **50**, 5528 (1994).
- ¹⁹ Shousuke Nakanishi and Masaru Tsukada Phys. Rev. Lett. **87**, 126801 (2001); Yanyang Zhang, Jiang-Ping Hu, B. A. Bernevig, X. R. Wang, and W. M. Liu, Phys. Rev. B **78**, 155413(2008).
- ²⁰ D. H. Lee, and J. D. Joannopoulos, Phys. Rev. B **23** 4997 (1981); J Zhang, QW Shi, J Yang, J. Chem. Phys. **120** 7733 (2004).
- ²¹ Rui-Lin Chu, Jian Li, J. K. Jain, and Shun-Qing Shen, arxiv: 0904.0678v1.